Optics & Laser Technology 169 (2024) 109964

Contents lists available at ScienceDirect

Optics and Laser Technology

journal homepage: www.elsevier.com/locate/optlastec

Full length article

Comprehensive benchmarking of laser welding technologies including novel beam shapes and wavelengths for e-drive copper hairpins

Simone D'Arcangelo [a], Leonardo Caprio [a], Davide Chesi [b], Daniele Nocciolini [b], Rubino Corbinelli [b], Barbara Previtali [a], Ali Gökhan Demir [a,*]

[a] Department of Mechanical Engineering, Politecnico di Milano, Via La Masa 1, 20156 Milan, Italy
[b] IMA Automation Atop, Strada S. Appiano 8/A, 50028 Barberino Tavarnelle, Italy

ARTICLE INFO

Keywords:
Electric motor
Copper welding
Green laser
Beam shaping
Hairpin winding
E-mobility

ABSTRACT

Laser welding is the industrially accepted method for the joining of Cu hairpin windings in the production of electric drives. High brilliance laser beams are scanned over the bare ends of the Cu wires producing a rapid connection through deep penetration remote welding. Despite being an accepted manufacturing method, laser welding of Cu hairpins still requires detailed studies concerning manufacturing productivity and quality. As the availability of novel laser sources with higher power levels, new wavelengths, and beam shaping capabilities increase, the need for benchmarking studies emerges. In this work, six different laser welding systems were compared in terms of process productivity and quality during the welding of Cu hairpins used for automotive traction. The different solutions presented power levels from 3 to 6 kW, with wavelengths from near infrared (NIR) to visible, including in source dynamic beam shaping. The weld bead formation was observed through high-speed imaging. The welds were analyzed in terms of their geometry, internal defects, and most relevantly for their mechanical strength. The results showed advantages of each of the employed system while the laser systems providing the highest irradiance profile produced the fastest weld with more elevated mechanical strength independently from the wavelength.

1. Introduction

As the regulations on the vehicle emissions is becoming more demanding, the electrification in mobility increases its pace [1]. While the automotive sector is leading the overall demand, the use of electric traction is expanding towards other land vehicles beyond automobiles such as trucks and vans. Following the demand, electrification is spreading also within naval and air transport. Especially in the automotive sector, the use of electric drives not only changes the emissions and the performance of the vehicle, but also the manufacturing chain involved [2]. Compared to a combustion engine the number of parts is reduced and the assembly process is mainly based on welding. The copper windings in the stator consist of the main welding application with the electric drive that requires hundreds of connections per part [3]. Laser welding is the industrially accepted method for providing these connections on the so-called Cu hairpins [4]. The use of the laser beam as a digital tool allows to flexibly plan the weld trajectory, adapt it to different product designs, and manipulate the bead size. Laser welding of Cu hairpins is indeed a clear example of how the laser based manufacturing processes play a key role in e-vehicle manufacturing [5]. The electric drives for automotive applications are essentially designed with laser welding processes in mind, rather than using laser as a substitution to a conventional manufacturing process [6].

Hairpins windings are widely used in electric drives substituting the conventionally used thin wire based windings. The use of thicker and solid sections allow to maximize the material usage in the given area, and hence, provide the means for carrying higher current flows [3]. The majority of hairpins are made of high purity Cu due to the high electrical conductivity, while Al hairpins are also used for applications requiring lower current flows. The hairpin windings require a dedicated process chain starting from a coiled product with an isolating layer. The wires are stripped from the isolator locally, cut to the required length, and deformed to the desired shape prior to the insertion to the stator. Once inserted in the position, the connections to generate the continuity of the winding is carried out on the exposed edges. Laser welding is used for providing the connection between the hairpins in an autogenous remote welding configuration. Commonly a high power laser beam is steered

* Corresponding author.
E-mail addresses: simone.darcangelo@mail.polimi.it (S. D'Arcangelo), leonardo.caprio@polimi.it (L. Caprio), davidechesi@atop.it (D. Chesi), danielenocciolini@atop.it (D. Nocciolini), rubinocorbinelli@atop.it (R. Corbinelli), barbara.previtali@polimi.it (B. Previtali), aligokhan.demir@polimi.it (A.G. Demir).

https://doi.org/10.1016/j.optlastec.2023.109964
Received 10 May 2023; Received in revised form 6 July 2023; Accepted 18 August 2023

Nomenclature

List of symbols

d_s	Spot diameter (μm)
h_f	Frontal height (mm)
t_f	Frontal thickness (mm)
h_l	Lateral height (mm)
w_l	Lateral width (mm)
w_t	Top width (mm)
t_t	Top thickness (mm)
a	Flange distance (mm)
d	Initial crosshead distance (mm)
l_c	Crosshead displacement (mm)
F	Tensile load (N)
F_{pk}	Peak load (N)
A_{tot}	Total area (mm^2)
A_{pore}	Pore area (mm^2)
A_{res}	Resistant area (mm^2)
φ	Porosity (%)
S_{app}	Apparent strength (MPa)
$\widetilde{\tau}$	Estimated shear strength (MPa)

with a scanner head over the exposed hairpins, generating a predetermined pattern. Such pattern can be linear [7], circular [8] or a combinations of these. The path is designed to expose both hairpins to the laser beam. Circular or elliptical patterns provide a continuous trajectory over the hairpins. However, the laser may reach the underlying polymeric isolator through the gap between the hairpins. Linear patterns on separate hairpins can potentially avoid exposing the underlying polymeric isolator with the expense of an intermittent heating process. Indeed, the weld pattern, laser intensity and scan speed are parameters that determine bead size as well as its shape. After the laser welding the joints are recoated with polymeric material to isolate the windings. In an electric drive for automotive applications the number of welds required can exceed 200. The avoidance of fasteners is highly advantageous for the simplicity of the electric drive compared to an internal combustion engine as well as saving weight. However, the large number of welds to be applied pose an important challenge both in terms of productivity and quality [9]. The performance of the welding operation has a direct consequence on the vehicle performance as it determines the current passage and the power provided by the electric drive [6]. In the last two decades the high brilliance solid state lasers such as fiber and disk sources have opened the way for reliable welding of Cu with high optical reflectivity [10]. On the other hand, the number of welds within the production of the electric drive render the process highly sensitive to defects such as porosity, blow out and spatter.

Deep penetration laser welding of Cu with high brilliance continuous wave (CW) fiber and disk laser sources with multiple kW laser powers is an established process [11]. At room temperature the optical absorptivity of pure Cu is approximately 2% at the wavelength of these laser sources emitting at 1 μm (typically $\lambda_{fiber} = 1070$ nm, $\lambda_{disk} = 1030$ nm) [12]. The high brilliance of the beams provide the means to initiate the process despite the low optical absorptivity by a generating a small fraction of melt, followed by vaporization, and keyhole formation [13]. Within the keyhole the laser is absorbed through multiple reflections increasing its apparent optical absorption [14]. Due to the high thermal conductivity and the intrinsic instability of the keyhole, deep penetration welding with 1 μm laser sources possesses instabilities related to spatter and porosity [15]. A valid strategy to remedy such issues is based on beam oscillation that helps to degas the welded seam and enlarges the melt pool [16]. Temporal power profile modulation [17] and the combined use of CW and PW (pulsed wave) emission [18] have also been shown to improve the welding stability with Cu-alloys. Conduction mode laser welding intrinsically provides a more stable weld pool, which can avoid pore and spatter formation [19]. Such conditions require a relatively larger laser beam and high power avoiding the generation of the keyhole. With 1 μm laser sources, stable conduction mode welding of Cu is not a viable option due to the very low absorption [11]. With the introduction of in-source dynamic beam shaping solutions, recent works proposed the use of novel irradiance profiles for the welding of the Cu hairpins [20].

The use of visible wavelength lasers has been recently made available to the industry in green [21] and blue wavelengths [22]. The low availability of such laser sources is related to their more difficult production route compared to the well-established fiber and disk sources. Green lasers are essentially fiber or disk lasers with harmonic generators operating at half the wavelength of the active media (ie. $\lambda = 515$ or 535 nm) [23]. Recently, the use of CW green laser have been shown to achieve conduction mode welding [24] as well as keyhole welding providing a wider spectrum of process window [25]. On the other hand, blue lasers are based on diode laser technology. The issues related to the blue diode lasers are power levels and beam sizes. The diode lasers have lower beam quality and are difficult to launch into small process fibers with high laser powers. Recently, the use of sub-kW laser power for welding Cu has been demonstrated with blue lasers [26].

Despite several choices in the laser welding technology, the fundamental studies concerning the laser welding of Cu hairpins and the influence of the laser processing conditions are limited in literature. Glaessel et al. studied [7] the laser welding of Cu hairpins with an 8 kW disk laser source and a 255 μm spot size using a linear trajectory. The authors proposed the initial relationships between seam size, electrical and mechanical properties. Dimatteo et al. studied laser welding of Cu hairpins with a 3 kW fiber laser source and a 68 μm spot size using a linear scan strategy with multiple repetitions [27]. The authors showed how defects form related to insufficient and excessive energy input into the seam. Omlor et al studied different scan strategies using a 6 kW disk laser with a 170 μm beam size [28]. On the other hand, several groups have attempted to consolidate the processing conditions through inline monitoring techniques with distinct conditions concerning the hairpin size, the employed laser source, and the processing conditions. In literature, process monitoring of laser hairpin welding is demonstrated using optical methods by means of photodiode intensity comparisons [29], optical coherence tomography for weld penetration measurements [30], and off-axis camera based solution for spatter analysis [31] to resolve single defects such as porosity, lack of penetration and material burst. Machine learning methods have been employed, however, concerning offline electrical conductivity measurements, optical 2D imaging [32] or 3D imaging after the execution of the weld [33].

With an increasing supply of new laser system solutions and an increasing global demand on the electric vehicles, the need for comparative studies identifying the quality measures and benchmarking different solutions is of great necessity. While scientific studies showing the optimization processes concerning a single laser technology are indeed required, those providing comparative analyses are absent. Indeed, benchmarking studies are lengthy and difficult in execution, since large experimental campaigns across different experimental systems should be considered. Indeed, the present work aims to respond to the need for a benchmarking work to compare the laser beam technologies in a fast-growing sector where scientific studies are scarce. To the authors' knowledge, no previous work has attempted to provide such a benchmark concerning laser welding of electric drive hairpins in particular, but also on any laser based manufacturing process for electric vehicles in general.

Accordingly, this work aims to provide a benchmark for the laser welding of Cu hairpins. The chosen hairpin size corresponds to those used in automotive traction. Bare Cu wires were welded using 6 different contemporary high brilliance laser technologies with power levels from 3 to 6 kW, with wavelengths from near infrared (NIR) to visible,

including in source dynamic beam shaping capability. The work describes in detail the experimental conditions, and the benchmarking criteria, as well as a critical analysis of the results employing analytical and statistical tools. Finally, the discussion provides an outlook on the advantages provided by each solution indicating improvement possibilities for future applications.

2. Materials and methods

In the benchmarking study, different laser beam technologies were identified and tested. The evaluated laser beam technologies are representative of solutions available in the catalogue of the major laser source providers, while a comparison between the providers was not the aim of this work. The related laser systems were available at different time instances thus the experimental work covered over a time period of one year. The main objective has been to assess the welding performance with process parameters providing sound welds in the desired dome form with sufficient penetration in the shortest process time. An overall optimization work between different laser sources was not within the aims of the present work. The optical chains were set mainly to achieve a desired spot size, while considerations regarding the scan field area, proximity to the welding region or the system size were not the primary concerns. In order to provide a comparative assessment, the welded hairpins were the same type and size in all the investigated conditions. The work was conducted using the same fixture type and the same characterization procedure. The systems analysed were chosen and tested as a function of their beam characteristics in terms of power, wavelength, and irradiance profile. All welds were carried out with systems operating at ideal conditions with clear optics, by an expert operator. While all geometrical characteristics of the welds were assessed after the welding operation, tensile tests were employed as the main indicator of weld quality.

2.1. Laser systems

In the benchmarking study six different laser welding configurations representative of the equipment currently available to the industry were evaluated. Table 1 reports the employed laser welding systems with their main characteristics. The systems were categorized for their power levels (mid or high), wavelength (NIR or green), spot size (d_s), and beam shaping capabilities (BS). For convenience, through the work each system is presented with its own tag as depicted in Table 1.

The first system "Mid power NIR, d_s=215 μm" (Mid-NIR-215) represents the established laser welding system based on 1 μm wavelength (λ = 1070 nm), medium power level at 4 kW and a relatively large spot size at 215 μm. In this work an active fiber laser was used for Mid-NIR-215, while the conditions are expected to be representative also for the disk sources with a similar wavelength (λ = 1030 nm). The second system "High power NIR, d_s=85 μm" (Hi-NIR-85) and "High power NIR, d_s=150 μm" (Hi-NIR-150) depicts higher power and smaller spot size allowed with a smaller fiber diameter using disk laser sources (λ = 1030 nm). The welding conditions are expected to be faster given the higher irradiance profile of the focused beam. The following conditions represent the use of dual core fibers for in-source dynamic beam shaping with high brilliance solid state lasers. "High power NIR, d_s=340 μm with beam shaping" (Hi-NIR-340-BS) and "High power NIR, d_s=600 μm with beam shaping" (Hi-NIR-600-BS) are provided from the same disk laser source (λ = 1030 nm) with different optical arrangements providing different spot sizes. The system is characterized by the internal and external fiber core diameter (ie. 50 μm and 200 μm). Such sources are expected to provide improvements in terms of pre- and post-heating in the scan trajectory, presumably providing a more stable melt pool. In this work the high power NIR systems were based on disk lasers, while the conditions are expected to be representative also for the fiber sources with a similar wavelength (λ = 1070 nm). Finally the "Mid power green, d_s=400 μm" (Mid-green-400) represents a different wavelength in the visible range operating at λ = 535 nm. This laser source was characterized by a larger fiber core at 200 μm. This source is expected to provide an improved absorptivity at the shorter wavelength, presumably providing a more efficient melting process. In this work the mid-power green laser systems were based on a disk laser with a second harmonic generator, while the conditions are expected to be representative also for the fiber sources with a similar wavelength. All systems were equipped with a scanner able to steer the beam and control the laser parameters with the desired scan pattern. At the time of the experimental work, the authors were not able to identify a blue laser system with sufficiently high power (>2 kW) and moderate spot size ($d_s \leq$ 400 μm). Such systems are expected to be commercialized in near future.

2.2. Material

In this work, hairpins with rectangular cross-section and smoothed edges typically employed in electric drives for automotive traction were used (see Fig. 1.a). The hairpin couples were put together along the longer edge corresponding to the hairpin width ensuring minimum gap formation by means of a dedicated clamp. Copper hairpins with 99.99% purity (ETP1/OF1 quality) without electrical insulation were used throughout the work. The bare material was selected to assess the influence of the laser welding capacity avoiding possible interactions and variations related to the isolation removal stage. The hairpin bars were characterized by a width of 3.87 ± 0.04 mm, a thickness of 2.66 ± 0.03 mm, and a corner radius of 0.67 ± 0.03 mm (intervals indicate average with respect to minimum and maximum values). The copper hairpins were cut from the coiled bars to obtain specimens with a length of 100 mm and a flat end.

2.3. Experimental conditions

The process parameters were set individually for each laser system in order to produce welds in the desired dome form with an average frontal weld bead height (h_f) above 3 mm (see Fig. 2) in the shortest overall process time. An elliptical scan strategy was used with all the employed systems (see Fig. 1.b). The maximum power levels were used for each of

Table 1
Main specification of the welding system employed.

System	Mid power NIR, d_s= 215 μm	High power NIR, d_s = 85 μm	High power NIR, d_s = 150 μm	High power NIR, d_s = 340 μm with beam shaping	High power NIR, d_s=600 μm with beam shaping	Mid power green, d_s=400 μm
Tag	Mid-NIR-215	Hi-NIR-85	Hi-NIR-150	Hi-NIR-340-BS	Hi-NIR-600-BS	Mid-green-400
Active medium	Active fiber	Disk	Disk	Disk	Disk	Disk
Wavelength, λ (nm)	1070	1030	1030	1030	1030	515
Max laser power, P_{max} (kW)	4	6	6	6	6	3
Fiber core, d_f (μm)	100	50	50	50/200	50/200	200
Collimation length, f_c (mm)	200	150	150	150	150	140
Focal length, f_f (mm)	300	255	450	255	450	265
Waist diameter, d_0 (μm)	150	85	150	85/340	150/600	380

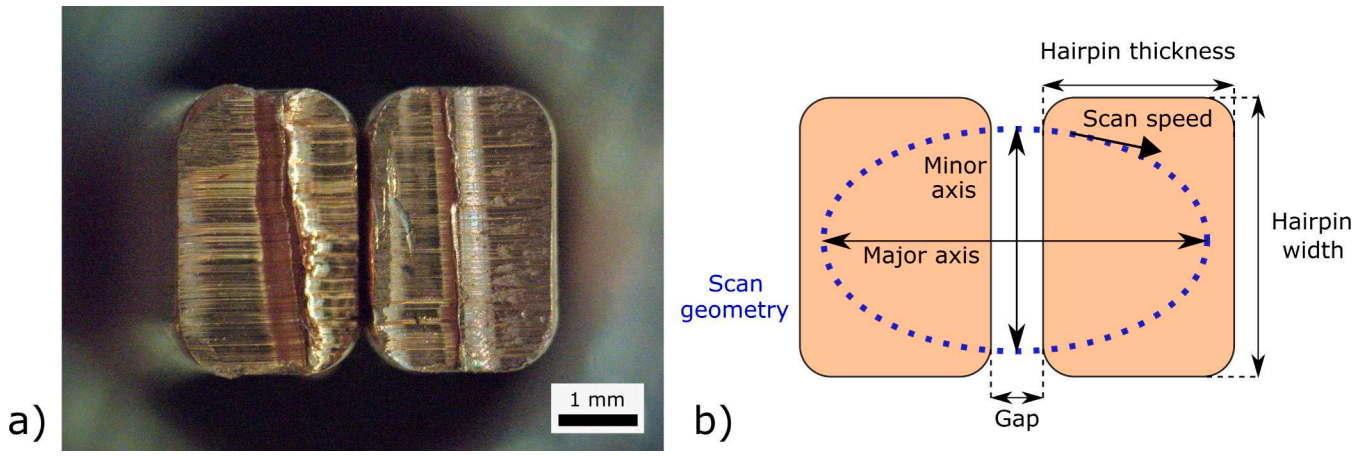

Fig. 1. a) Top view of the hairpins positioned in the clamping system and b) schematic view of the scan geometry.

the available system, while the weld speed and the scan loop number were set to provide a the desired weld bead height. The peak irradiation (I_0) of the employed beams were calculated assuming a Gaussian-like distribution in the central core of the delivery fibers using the following equation,

$$I_0 = \frac{8P}{\pi d_s^2} \tag{1}$$

where P is the power in the central core (with multiple cores the power in the central core was considered). The cycle time (t_{cycle}) and total energy inputs (E_{tot}) were calculated as general indicators of the processing conditions with the following equations

$$t_{cycle} = \frac{CN}{v} \tag{2}$$

$$E_{tot} = Pt_{cycle} \tag{3}$$

where C is the circumference of the scanned elliptical trajectory, N is the applied number of scan loops and v is the scan speed.

Table 2 shows the chosen process parameters for each laser welding system. In the chosen conditions for the benchmarking study, the Mid-NIR-215 system required a moderate welding speed at 217 mm/s and 5 scan loops. The relatively low peak irradiance of the system at 22.2 MW/cm^2 requires 245 ms cycle time and 980 J total energy input. The Hi-NIR-85 system improves the weld speed to 430 mm/s with 5 loops. The much higher peak irradiance at 211.5 MW/cm^2 allowed to execute the weld at 135 ms using 810 J total energy. The Hi-NIR-150 system maintained the scan speed and cycle loops at 430 mm/s and 5 respectively. Despite a lower peak irradiance at 67.9 MW/cm^2, the cycle time and the total energy input were the same as the previous case. The use of in-source dynamic beam shaping required the sharing of the total laser power between the central core and the ring. For the system with in-source dynamic beam shaping, the elliptical trajectory was slightly reduced in order to accommodate the larger beam size in the ring part.

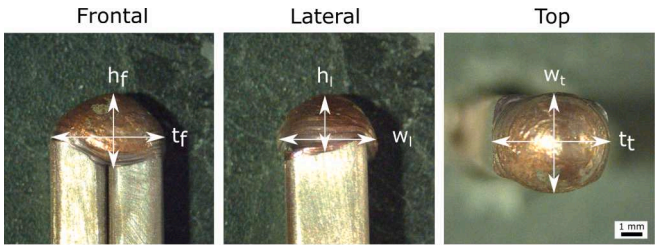

Fig. 2. Schematic description of the weld seam geometry measurements.

The Hi-NIR-340-BS system consisted in a small central spot diameter at 85 μm having 35% of the total power of 6 kW, while ring with spot size of 340 μm received the remaining 3.9 kW. The peak irradiance was 74 MW/cm^2. In this condition the welding speed was relatively high at 300 mm/s, however, requiring 6 loops. Resultantly the cycle time was 160 ms with a total energy input of 960 J. The Hi-NIR-600-BS condition followed the same approach as Hi-NIR-340-BS, except the power distribution between central core and ring as well as the final spot size. The 6 kW power was divided equally between the central core and the ring producing a 150 μm spot in the centre and 600 μm in the ring. The peak irradiance was consequently reduced to 34 MW/cm^2. The cycle time and the total energy remained unvaried with respect to Hi-NIR-340-BS. Finally, the Mid-green-400 condition required a relatively slow weld speed at 100 mm/s with a reduced number of scan loops (N = 4). In this condition the lowest overall peak irradiance was employed at 4.8 MW/cm^2, producing the welds at 550 ms employing 1650 J total energy.

During the benchmarking study, the specimens were carefully set in position using a dedicated fixture allowing to minimize gap (<50 μm). The statistical study has been carefully designed and conducted. Prior to the experiments the number of replications was evaluated to assess the power of the statistical test used in the analysis of variance (ANOVA). In order to have a power of the statistical test above 90% considering a difference between groups corresponding twice the standard deviation, 10 replications were required per each of the 6 laser systems employed [34]. Hence at least 10 replications were produced for each of the employed systems. ANOVA was applied to the main process output peak force in the tensile tests with a statistical significance level of α = 5%.

2.4. Characterization

2.4.1. High speed imaging

High speed imaging was carried out during the welding operation with the Mid-NIR-215 system with a CMOS based system (Phantom High Speed VEO-E 310L, Vision Research, Wayne, NJ, USA). The camera was placed in an off-axis configuration with respect to the weld region, the image field facing the shorter side of each hairpin at an angle of approximately 20° with respect to the surface normal. External illumination and the received light was filtered at 660 ± 10 nm to suppress the process light. Images were acquired at 10,000 frames per second and analysed qualitatively to assess melt pool formation and the solidification phenomenon.

2.4.2. Weld geometry

The weld geometry was assessed in detail in the frontal, lateral, and top sides of the beads as shown in Fig. 2. Optical microscopy (8M−B6/SM 353H, EchoLab, Paderno Dugnano, Italy) images of each welded

Table 2
Parameter combinations used for each laser system in the benchmarking study.

System	Mid power NIR, d_s=215 µm	High power NIR, d_s = 85 µm	High power NIR, d_s = 150 µm	High power NIR, d_s = 340 µm with beam shaping	High power NIR, d_s=600 µm with beam shaping	Mid power green, d_s=400 µm
Tag	Mid-NIR-215	Hi-NIR-85	Hi-NIR-150	Hi-NIR-340-BS	Hi-NIR-600-BS	Mid-green-400
Laser power, P (kW)	4	6	6	6 (2.1 centre + 3.9 ring)	6 (3 centre + 3 ring)	3
Focal position, Δz (mm)	+1.5	0	0	0	0	+1.5
Spot diameter, d_s (µm)	215	85	150	85/340	150/600	400
Scan speed, v (mm/s)	217	430	430	300	310	100
Scan strategy	Elliptical	Elliptical	Elliptical	Elliptical	Elliptical	Elliptical
Scan dimensions (mm × mm)	4.3 × 2.3	3.8 × 2.0	3.8 × 2.0	3.8 × 2.0	3.8 × 2.0	4.8 × 3.3
Scan loop, N	5	5	5	6	6	4
Peak irradiance, I_0 (MW/cm^2)	22.2	211.5	67.9	74.0	34.0	4.8
Cycle time, t_{cycle} (ms)	245	135	135	160	160	550
Total energy, E_{tot} (J)	980	810	810	960	960	1650

specimen were taken from the three viewpoints. Frontal dead height (h_f) and thickness (t_f), lateral bead height (h_l) and width (w_l), and top width (w_t) and thickness (t_t) were assessed separately.

2.4.3. Mechanical testing

Mechanical peel test was carried out following the reference standard BS EN ISO 14270:2016. As shown in Fig. 3.a, the welded specimens were bent to achieve a flange length of 15 mm and a crosshead distance of 70 mm using a dedicated die. The tests were carried out using a universal testing machine (MTS 1kN) and a peel velocity of 10 mm/min. The pull force applied to the weld was recorded as a function of the crosshead position. The peak load (F_{pk}) was observed once the weld bead failure started, followed by a successive fracture load occurring at the separation point (Fig. 3.b). For the functioning of the electric drives, the peak load constitutes an important factor. The hairpins are expected to withstand forces and vibrations exerted on the electric drive through the use of the vehicle. The mechanical resistance of the hairpins can also be a proxy for the electrical conductivity of the connections[7]. However, the critical point remains the mechanical integrity as a sufficient electrical connection can also be achieved with a mechanically less resistant weld.

2.4.4. Porosity in the fracture surfaces

In the laser welded hairpins porosity is a well-known issue. The pores in the weld seam can be generated due to the keyhole instabilities as well as entrapment of the isolating material. In the absence of the isolating material, the analysis of porosity is expected to be representative of the keyhole instabilities and hence a more direct indicator of the laser welding performance. Porosity can be analysed via metallographic cross-sections or X-ray tomography. Metallographic cross-sections provide a direct visualization of pore geometry and size at a given position and is a destructive method. Hence, it is suited to assess the porosity for a sampled population. X-ray tomography can provide a 3D reconstruction of the weld seam showing the distribution and the size of pores in the seam. Despite being a non-destructive method, X-ray imaging is a slower method for characterizing a large number of welds and difficult to be implemented as control method on e-drive production lines.

In this work, the porosity was evaluated on the fracture surfaces as an indicator of the failure mechanism. As shown in Fig. 4, optical microscopy images of the fracture surfaces were taken from a normal projection of the surface. By using image processing software (ImageJ, Bethesda, USA) the total area of pores (A_{pore}) was measured to assess porosity using the following equation:

$$\varphi = \frac{A_{pore}}{A_{tot}} \tag{4}$$

where the total area of the seam (A_{tot}). The resistant area (A_{res}) was calculated by subtracting the total area of pores from the total area of the seam as expressed in the following equation:

$$A_{res} = A_{tot} - A_{pore} \tag{5}$$

The use of the resistant area allowed to determine the influence of

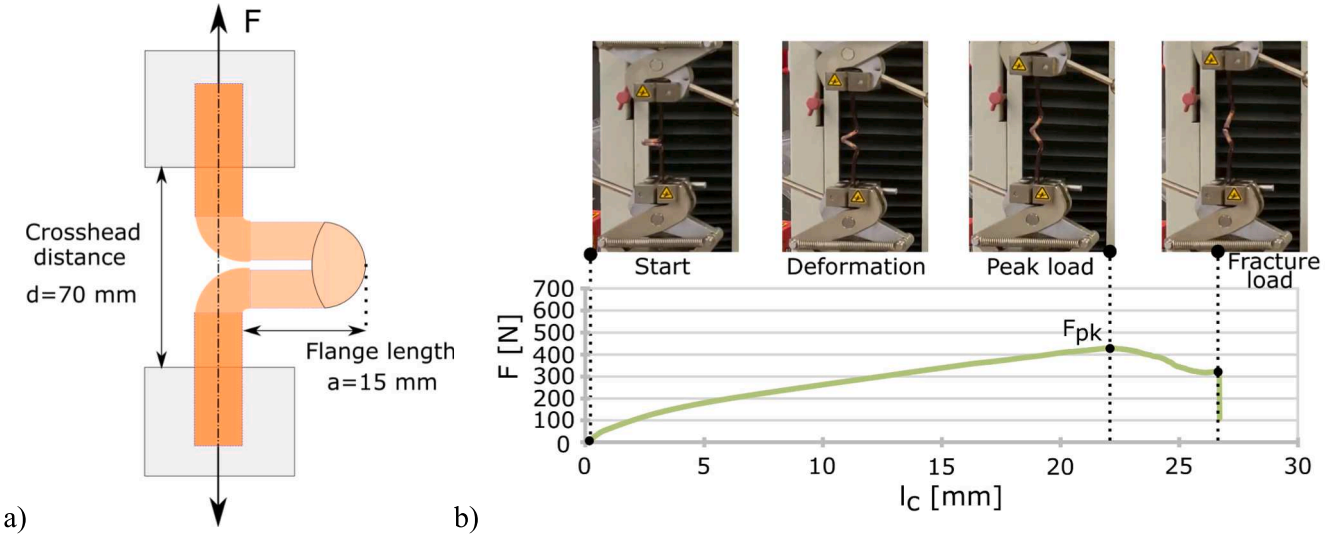

Fig. 3. A) Schematic description of the mechanical testing configuration. b) typical force-distance curve during the mechanical testing of the hairpins showing the critical instances.

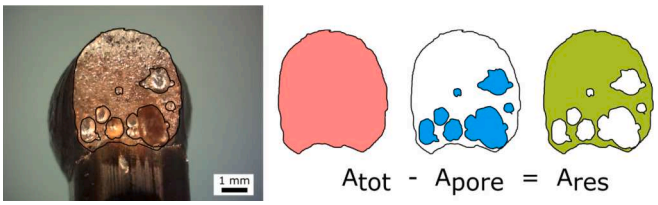

Fig. 4. Schematic description of the porosity and the effective resistant section measurements taken on the fracture surfaces.

the melting capacity and the pore quantity together as a function of the employed laser systems. Additionally, computed X-ray tomography was used on selected samples to assess the pore distribution qualitatively (X25 MicroCT, North Star Imaging, Rogers, MN, USA). The voxel size of the acquisitions was 14.3 × 14.3 × 14.3 μm^3.

3. Results

3.1. Formation of the weld bead observed via high speed imaging

Fig. 5 shows excerpts from the high speed videos during the laser welding of the hairpins with the Mid-NIR-215 system. The images show the critical time instances during the process. In Fig. 5, the process start can be seen, where the laser ignition corresponds to an almost immediate formation of the keyhole. In Fig. 5.b, the end of the first loop is seen, where the weld seam is solidified behind the laser beam. In this condition, the laser beam interacts with solid Cu with the keyhole welding modality. At the end of the second loop shown in Fig. 5.c, the melt pool starts to elongate and remains open also behind the laser beam. By the end of the 3rd loop the melt pool fronts are unified and the laser beam interacts with the liquid Cu. In the 4th loop of Fig. 5.e and the 5th loop in Fig. 5.f the laser beam interacts with liquid Cu increasing the size of the molten material, while the surface tension tends to form the semi-spherical bead shape. After the turn off of the laser source as seen in Fig. 5.g the material starts solidifying from the hairpins towards the farthest point of the bead. During the solidification duration, small bubbles of gas are observed exiting from the molten region at the top. At approximately 550 ms, hence 305 ms after the end of the laser emission, the melt material is completely solidified. The images indicate that the process changes significantly between consecutive loops from a conventional keyhole welding towards a melt stirring operation. The number of loops after the formation of the complete melt pool over the hairpin surfaces allow increasing the melt fraction and weld depth. The heat input and temperature gradients are expected to determine the final shape of the bead. Excessive loops were found to deteriorate as observed with the violent expulsion of the material. Insufficient number of loops instead produced shallow and incomplete bead formation.

3.2. Weld bead morphology

Fig. 6 shows representative images of the welded hairpins with different laser systems from frontal, lateral, top views. All systems allowed to complete the welding process without macroscopic defects with the formation of the characteristic semi-spherical weld bead. The weld morphology and the sizes were observed to be different as a function of the employed system. Once again the Mid-NIR-215 system can be taken as the reference, where the weld bead appears to fully cover the two hairpins. The maximum depth is observed at the junction of the two hairpins following an elliptical form seen in the frontal view. The Hi-NIR-85 conditions shows a more abundant melt material volume. The weld bead covered both the welded hairpins and slightly exceeds the total width. The maximum depth is once again in the central point, while the bead form tends to move towards a teardrop shape. The Hi-NIR-150 has a similar bead morphology with the Hi-NIR-150 with a smaller melt volume. With Hi-NIR-340-BS and Hi-NIR-600-BS the weld bead morphology tended to flatten. In the top view, it is seen that the external edges remained not completely melted, which can be attributed to the reduced scan trajectory. Finally, with Mid-green-400 the welded beads were abundant in volume expanding laterally. The increased melt material fraction appears to form a circular melt pool as seen in the top view. The weld bead remains flat on the interface between the bead and the hairpins. The images indicate that while all conditions provide satisfactory results from a qualitative viewpoint, the employed laser systems may provide very different results in terms of bead morphology.

3.3. Weld seam height, width, and thickness

Fig. 7 shows the measurements of the weld geometrical attributes belonging to the different welding systems. Coherently to the weld bead observations, the resultant weld geometries were found to be comparable. The front weld thickness (t_f) was found to be above 5 mm in

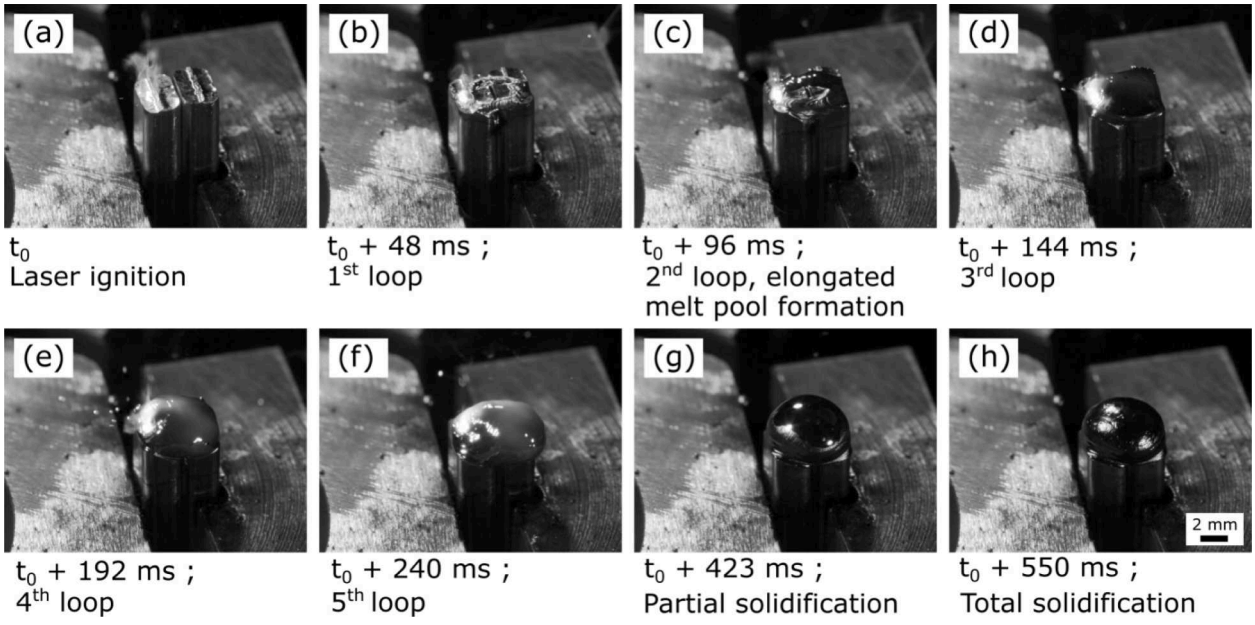

Fig. 5. Critical time instances showing the formation of the weld bead during the laser welding of hairpins with the Mid-NIR-215 system.

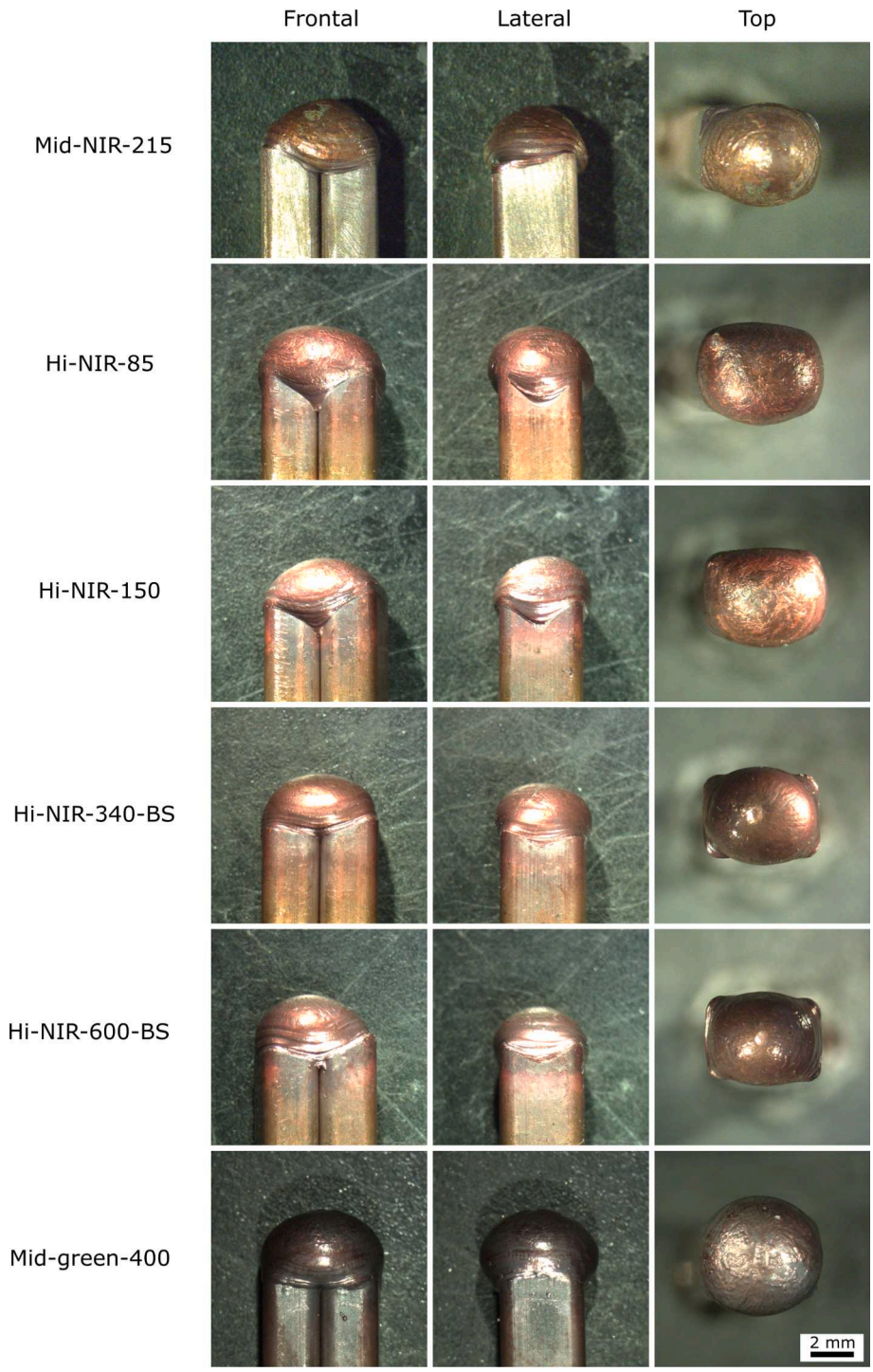

Fig. 6. Macro images of the produced specimens using the different laser systems.

average, hence covering both the hairpins. The Hi-NIR-85 condition provided the biggest value of t_f, while beam shaping systems had the lowest thickness as expected to be due to the smaller weld trajectory. The front weld height h_f varied between 3 and 4 mm between the different systems. The highest h_f was found with Hi-NIR-85, while the beam shaping conditions provided the smallest ones. The reduction of the peak irradiance accompanied with a reduced total energy is expected to reduce the weld height with beam shaping conditions. The lateral width w_l was found to be adequate for all conditions covering the width of both the hairpins. The height value of w_l was observed with Mid-green-400. The wider spread of w_l in this condition can be attributed to high total energy and cycle time resulting in a sagging of the weld bead in time. Hi-NIR-600-BS provided the smallest width once again owing to a smaller peak irradiance and a smaller scan track. The overall trend of lateral height h_l was similar to that of h_t. However, it was noted that lateral height was approximately 0.5 mm lower in all cases, indicating that melting depth is expected to be larger around the central part of the bead. Concerning the top thickness t_t, all conditions were found to be once again larger than the combination of the hairpin thicknesses. The highest value of t_t was observed with Hi-NIR-85. On the other hand the values of t_t and t_f were very similar for Mid-green-400, once again indicating the influence of the long weld process resulting in a more

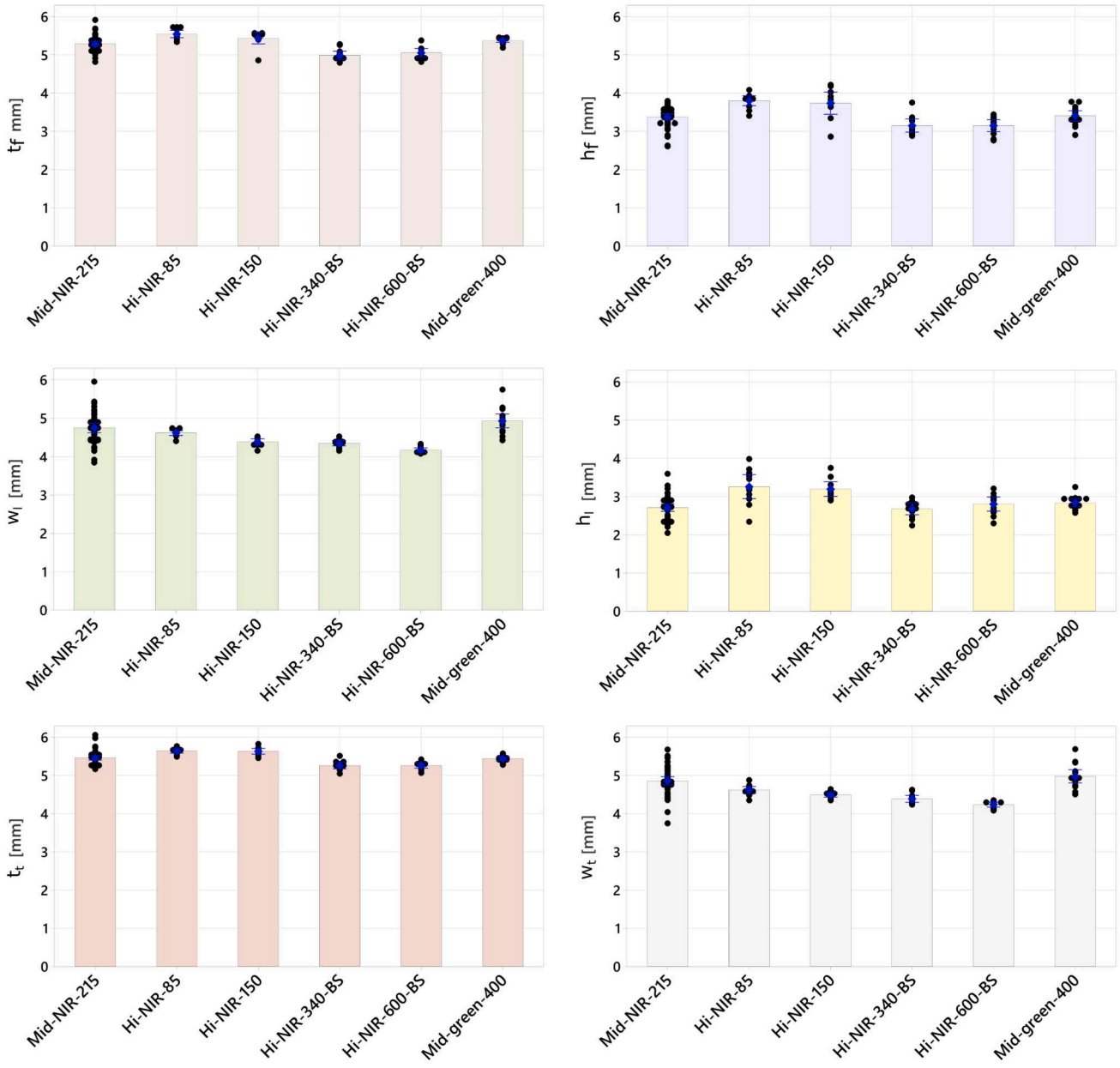

Fig. 7. Weld seam height (front h_f and lateral h_l), width (lateral w_l and top w_t), and thickness (front t_f and top t_t) measurements for the different laser systems used. Error bars depict standard error.

symmetrical bead. Finally, the top width w_t was found to be the largest with Mid-green-440, indicator of a wide spread. The lowest values of w_t were with Hi-NIR-600-BS, coherent with the previous observations on the smaller trajectory and the reduced peak irradiance.

3.4. Mechanical resistance of the welded hairpins

Fig. 8 shows the tensile test curves of the specimens produced with the different laser systems. In order to depict the representative test curve of each laser system, the test producing the median value of the F_{pk} is highlighted in red, while the other curves are shown in grey to depict the variability. The overall results show that the laser system has an influence on the peak force as well as the tensile behaviour. In most of the conditions, the peak force was observed prior to the fracture completion. In the case of Hi-NIR-85, the fracture appeared to occur of at the peak force. In the case of the other laser systems, the forces increased as the bent arms of the tensile specimens are flattened. The fracture started commonly at the bottom of the weld bead close to a shear dominant action generating a drop in the force as the crosshead moves. Then the fracture propagated leading to the completion of the fracture at a lower force. In the case of Hi-NIR-85, the fracture often did not appear to start before the bent arms were fully straightened. The forces increased to the point of fracture dropping down continuously after on. Such conditions are expected to be closer to a complete tensile action on the weld bead. This phenomenon was accompanied by higher peak forces compared to the other laser systems.

Fig. 9 reports the peak forces as a function of the employed laser system. It can be seen that the Hi-NIR-85 stands out with the highest average peak force at approximately 400 N. Mid-NIR-215, Hi-NIR-150, Hi-NIR-340-BS, and Hi-NIR-340-BS showed similar average peak forces

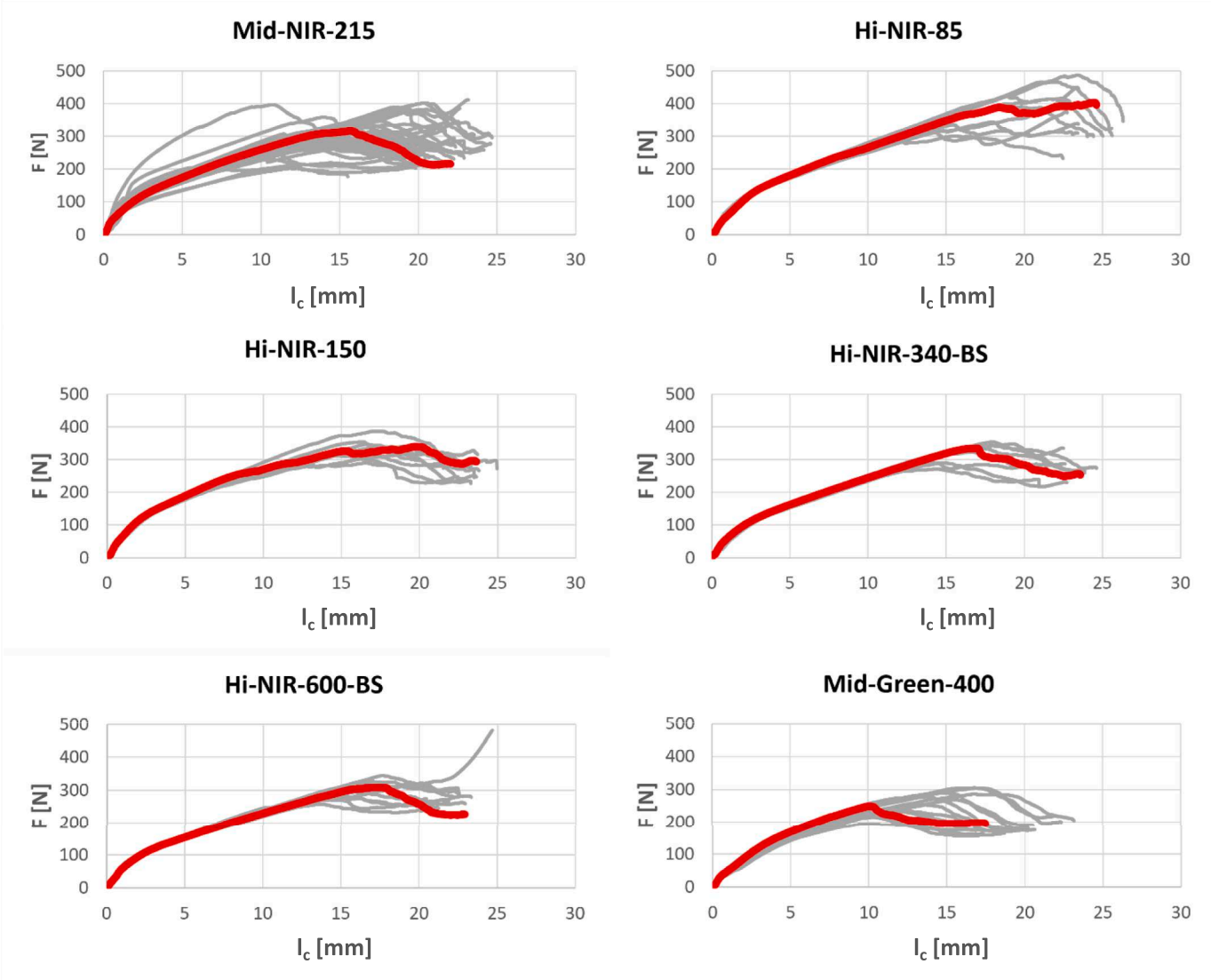

Fig. 8. Tensile curves of the laser welded hairpins using the different laser systems. The curve highlighted in red of each panel represents the test producing the median F_{pk} of employed laser system, while the grey curves represent the rest of the tests.

at approximately 320 N. The Mid-green-400 condition was characterized by a relatively lower peak force at approximately 250 N.

Table 3 shows the ANOVA table for the peak force measurements. Note that the sample size for the different groups were different due to the material availability. The analysis confirm that the laser system has a significant influence on the peak force. At this point Tukey comparison between the means was carried out to assess the difference between the groups. Fig. 10 graphically represents the different groups. It can be seen that Hi-NIR-85 provides the highest peak force in average, and it is statistically different from the rest. Mid-NIR-215, Hi-NIR-150, Hi-NIR-340-BS and Hi-NIR-600-BS were statistically found provide the same average peak force. Finally, the average peak force of Hi-NIR-600-BS and Mid-green-400 were found to be of the same group, resulting to be the lowest peak force observed. The results confirm that the highest intensity beam providing the least total energy at the fastest processing time provided the strongest joint of the hairpins.

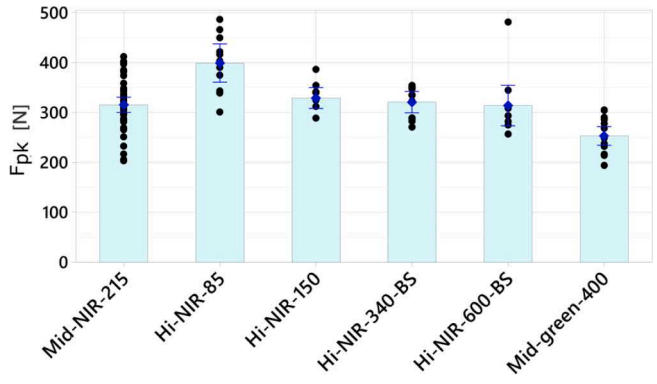

Fig. 9. Peak load of the tested conditions. Error bars depict standard error.

An important factor regards the identification of a possible correlation between the external geometrical attributes and the mechanical strength of the weld beads. Fig. 11 shows the scatter plots between the dimensions of the weld bead and the peak force, while Table 4 shows the

Table 3
ANOVA table for peak force (F_{pk}).

Source	DF	Adj SS	Adj MS	F-Value	P-Value
System	5	140,855	28,171	14.68	0.000
Error	96	184,166	1918		
Total	101	325,021			

Fig. 10. Tukey comparisons between the different systems. The laser systems that do not share a letter possess statistically different mechanical properties.

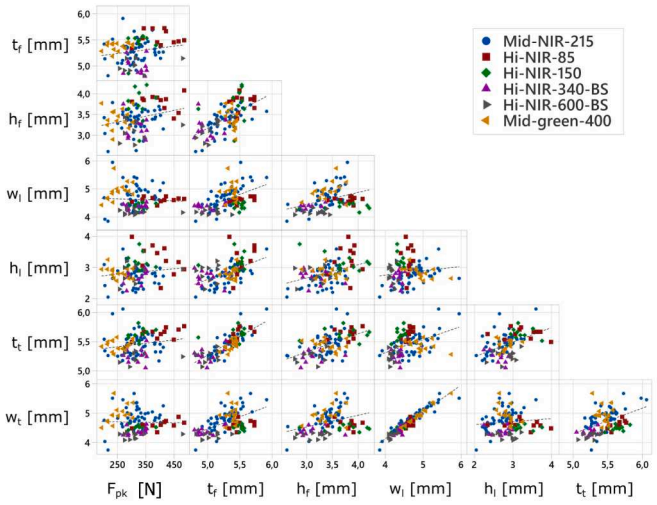

Fig. 11. Correlation between the dimensions of the weld bead and the peak force. Dashed lines indicate trend.

correlation coefficients. Coherent to the qualitative observations, some of the geometrical attributes have strong correlation levels. Thickness and width measurements in different are strongly correlated (ie. t_f with t_t; w_f with w_t) with coefficients above 0.8. On the other hand, the frontal and lateral bead heights (h_f with h_l) do not show a clear correlation with a coefficient at 0.394. Evidently, the weld penetration varies along the bead with the applied conditions and the chosen scan strategy. More importantly in the analysed conditions, none of the weld geometry indicators provide a direct correlation with the peak force. The biggest correlation factor with the peak force is at 0.249 with lateral height (h_l). A single geometrical indicator is not able to describe the mechanical behaviour, especially considering that all the benchmarked conditions provided welds free of external macroscopic defects. Once again, this is attributed to the presence of internal pores and the variability of the resistant area within the weld bead. However, the presented data can be of further use for classification purposes and machine learning approaches.

3.5. Porosity measured on the fracture surfaces

Fig. 12 shows an image that compares the porosity in the fracture surface and the porosity revealed by the X-ray CT scan starting from the bare Cu hairpins (Fig. 12.a). It can be seen that the pores of larger dimensions extending to 1 mm in diameter are accumulated in the bottom (Fig. 12.b). The dimensions of the pores tend to reduce towards the

Table 4
Correlation coefficients between the dimensions of the weld bead and the peak force.

	F_{pk} [N]	t_f [mm]	h_f [mm]	w_l [mm]	h_l [mm]	t_t [mm]
t_f [mm]	0.173					
h_f [mm]	0.249	0.605				
w_l [mm]	−0.053	0.533	0.374			
h_l [mm]	0.145	0.518	0.394	0.147		
t_t [mm]	0.183	*0.806*	0.547	0.455	0.476	
w_t [mm]	−0.029	0.540	0.358	*0.953*	0.100	0.446

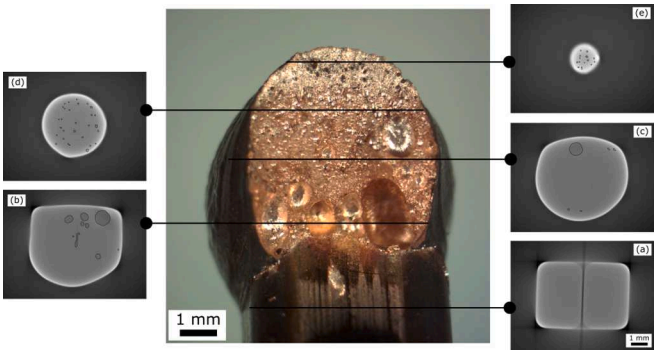

Fig. 12. Representative X-ray scan of a laser welded hairpin showing the distribution of the pores produced using Mid-NIR-215 configuration. The lines show where each X-ray slice has been taken.

upper part of the weld bead (Fig. 12.c). Approaching towards the upper regions of the bead the number of pores increase and with diameters in the range of 10–100 μm (Fig. 12.d). These small pores remain entrapped under the solidification skin at the very top of the bead (Fig. 12.e). The dimensions and the distribution of the pores provide insights to the process dynamics. It can be expected that the large pores are related to the keyhole instabilities as observed by Heider et al.[15].. As discussed always by Heider et al. such pores are caused by the loss of equilibrium between the capillary and recoil pressure forces acting on the bottom of the keyhole which eventually leads to the gas entrapment phenomenon that consolidates as porosity due to the rapid solidification. The smaller pores could be caused by the splitting of the larger pores caused by the multiple scans or by the elevated solubility of copper at elevated temperatures. Such phenomenon is well known in conventional casting process of Copper as mentioned by Monroe[35]. As a matter of fact, gas ejections were observed also in the high speed images. Evidently, the keyhole width and stability, melt lifetime, and cooling rates play a key role in the formation of the pores.

Fig. 13 shows representative images of the fracture surfaces obtained with different laser systems. It can be seen that the larges pores are always present at the bottom of the seam and the fracture appears to have initiated from these points. Moreover, the fracture surface shape and size appear different as a function of the laser system. With Mid-NIR-215, Hi-NIR-340-BS, and Hi-NIR-600-BS a relatively circular fracture bead is visible. With Hi-NIR-85 and Hi-NIR-150 the bottom side of the bead appears to have concave shape with the two edges penetrating deeper into the material. Such geometry is expected to be due to the high peak irradiance without the presence of a ring beam. Finally the fracture surface of Mid-green-400 appears to have a flatter and shallower bottom, expected to be due to the low irradiance level.

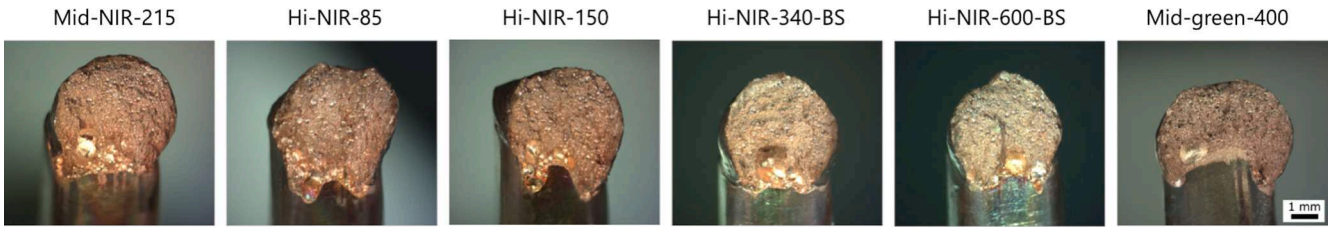

Fig. 13. Representative images fracture surfaces of the weld beads produced with the different laser systems.

Fig. 14 shows the porosity measurements on the fracture surfaces. It can be seen that the average porosity values vary between 7 and 15%, while a large variability is viewed in all the employed systems. The lowest porosity levels appear with Mid-green-400, while the highest with Hi-NIR-85. It can be attributed that a fast welding process with a high peak irradiance provides shorter time for the porosity to be split and degassed through the melt pool. On the other hand, the porosity levels do not match the trend observed with the peak forces of the mechanical tests. These observations underline the necessity to analyse the bead section and the porosity together.

Fig. 15a shows the porosity of the specimens with respect to the peak force of the tensile tests. It can be seen that the porosity does not appear to be directly correlated with the mechanical behaviour. Indeed, the internal defects and the weld bead size are both influenced by the employed laser system. Hence, the porosity values are not sufficient to explain the mechanical resistance in terms of the peak load to failure on their own. Fig. 15.b depicts the resistant area measurements against the peak force of the tensile tests grouped for each laser system. Despite the dispersion of the data a clear trend appears to exist, as the increase of the resistant area improves the mechanical strength of the joint. The regression fit using all the data point can be used to interpret the mechanical strength of the weld bead. The fitted model equation was found as:

$$F_{pk} = S_{app} A_{res} \tag{5}$$

where S_{app} is the apparent strength to the mechanical test with a value of 29.9 ± 1.0 MPa within 95% confidence interval for the mean. The fitted model was found adequate with an R^2_{adj} at 97.1%, while respecting all the hypotheses. The final shape of the specimens after the mechanical test can be interpreted to have a first approximation of the shear strength of the welds. The top of the weld bead can be considered the hinge point, while the bottom of the bead as the region where the shear moment is applied. The measurements show an amplification of 3 to 4 concerning the moment arm generated at the direction where the peel force is applied. Hence, an estimated shear strength can be calculated at $\tilde{\tau}$ = 120–160 MPa. The tensile strength of pure Cu is 180–260 MPa with a yield strength at 30–60 MPa [7]. Hence the approximate shear strength would correspond on average 64% of the tensile strength. Chen et al. observed that the laser welded pure Cu specimens with negligible porosity in the seam had a tensile strength reduction from 180 MPa 160 MPa [36]. Eisenreich et al. identified the shear strength of laser welded thin sheets at approximately 180 MPa [37]. Indeed a direct comparison between the observed apparent strength and the values shown in literature is very difficult especially due to the complex stress field generated during the applied mechanical test. The results suggest a reduction in the material strength due to the internal defects, microstructural changes expected due to the multiple laser scans. However, it can be concluded that the porosity levels can be encountered by increasing the weld penetration. The data dispersion can be related to the changes in the material properties in terms of microstructure, which was not within the main aims of this work. The weld duration and beam intensity are expected to induce different effects on the material properties from the bed to the base material as the pure Cu has a very low annealing temperature (approximately 400 °C). It should be noted that the static resistance of the material is a proxy to its mechanical behaviour and the electrical stability. The weld bead shape and the porosity levels are expected to play an important role on the fatigue behaviour as well.

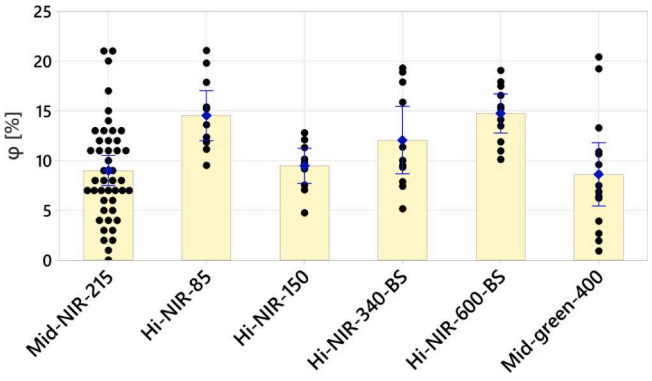

Fig. 14. Porosity levels on the fracture surfaces of the hairpins welded by different systems.

4. Discussion

The results provide several insights to the laser welding of Cu hairpins. Despite the principal differences in the employed laser systems, the work puts together the main comparison factors both between the laser systems and the obtained welds. The main outcome of the work is that all contemporary solid state laser sources are capable of executing the laser welding operation of copper hairpins. The work evaluated the mechanical strength as the key factor determining the quality of the weld considering that all the laser sources provided welds without any macro defects. Within the analysed laser systems, the one that provided the fastest process also yielded the highest strength. The Hi-NIR-85 condition points out the necessity to have a high irradiance profile to initiate and maintain a deep keyhole. The results confirm that in keyhole welding mode the determining factor is the irradiance rather than the optical absorptivity at the ambient temperature. Once the keyhole is formed, the laser power is absorbed via multiple reflections moving towards a much higher apparent optical absorptivity [38]. It was seen that the laser welding time required to achieve a given weld height mainly depended on the peak irradiance whilst remaining independent from the wavelength. This is in accordance with the results reported by Hummel et al. that showed that when employing green and NIR sources in keyhole processing conditions the absorptivity is comparable [12]. Hence, taking into account the mechanical performance of the joints, the use of a visible wavelength does not appear to provide a significant improvement in the deep penetration welding of Cu hairpins. As a matter of fact the green wavelength employed is generated from a NIR source with twice the laser power. As anticipated by Hummel *et al.*, the present work suggest that it may be preferable to employ a high peak irradiance exploiting the full power available of NIR laser sources rather than employing visible wavelength emission [12]. The use of visible wavelengths may indeed be of considerable advantage concerning smaller thicknesses, where high peak intensities are not required for

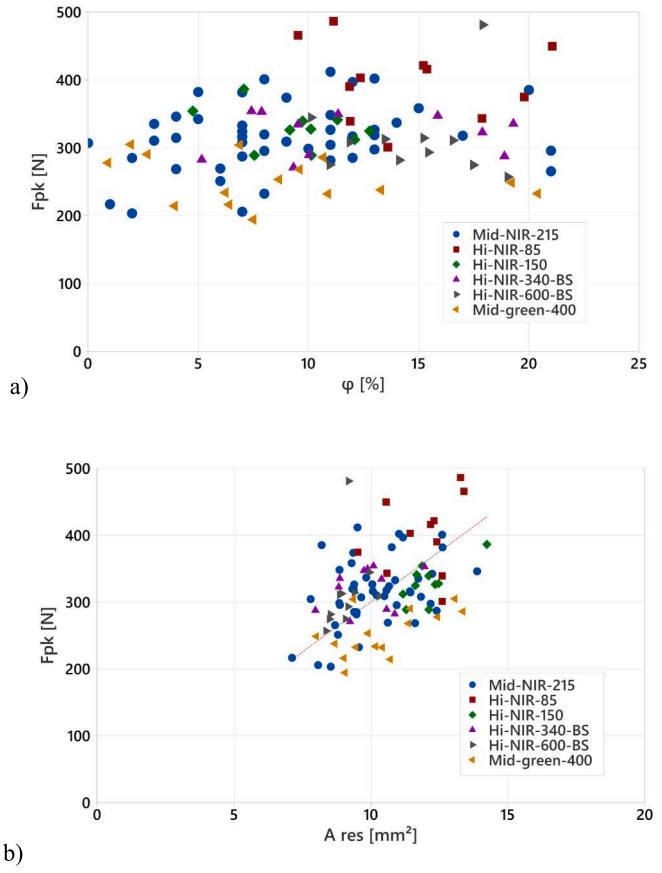

Fig. 15. a) Porosity and the peak load of the tested specimens. b) Correlation between the effective resistant area and the peak load. Dashed line indicates the linear regression fit.

generating large weld seams. Concerning the beam shaping options tested in this work, it was seen that the sharing of the total laser power between the central core and the ring results in a reduction of the penetration, similar to what has been observed with stainless steel [39]. The results suggest that it may be preferrable to maintain the high peak irradiance and add power to the ring in order to combine the deep welding effect at high processing speeds and benefit from spatter suppression. Such configuration would potentially consider a comprehensive laser power of approximately 8–9 kW. On the other hand, the use of visible wavelengths may come in handy to achieve a conduction mode heating on pure Cu. Avoiding the use of keyhole formation can be beneficial to reduce the porosity. In terms of a more efficient energy conversion, blue diode lasers can provide benefits. Not needing wavelength conversion, the complete laser power would be used on the workpiece. Such solutions will require also potentially smaller delivery fibers and the development of high power optics for this wavelength. Recent solutions indicate power levels up to 3 kW with 400 μm fiber diameter [22], or 400 W with 50 μm fiber diameter [40]. Wavelength combinations (NIR + visible) with industrial solid state lasers [41], using green and NIR [42], as well as blue and NIR [43] are other possibilities that require fundamental studies to understand the possible benefits for industrial development for the given material/thickness combination.

Within the present work the influence of gap, misalignment, and the residual isolating material was not assessed. Indeed, a laser system that is resilient to such issues is preferrable. The use of inline monitoring solutions for seam finding, gap and misalignment measurements are essential for the production of the entire e-drive [30]. In the presence of such issues, the use of dedicated parameter sets able to avoid the weld macro defects such as melt ejection or burst of the entire bead can be envisaged. From this perspective, the use of in-source beam dynamic beam shaping can provide further advantages with a wider range of parameter selection [44]. The influence of the residual isolating material also points to the performance of the stripping process [8]. Often the isolator removal is carried out by laser stripping [45], whose performance is expected to have a direct impact on the welding process that requires further investigations. The use of inline monitoring signals to assess weld quality classification [46] or the weld mechanical behaviour [47] are other strategies that would improve the reliability of the manufacturing process over the entire stator as well as the continued production.

Beyond the influence of the laser parameters, the employed systems may differ in terms of cost, energy consumption, reliability, maintenance, and footprint. Such conditions may have a direct impact on the final choice of configuration, while their analysis is beyond the scope of this work. On the other hand, the benchmarking work underlines that the competitiveness and the level of advancement that the solid-state fiber and disk laser sources have achieved. Several options for spatial and temporal beam shaping techniques as well as novel wavelengths become available as the technology further progresses. Indeed, the e-vehicle manufacturing sector follows an ever-increasing pace, which pushes the product requirements and process economy to more demanding levels. From this perspective the availability of open benchmarking data will remain greatly important.

5. Conclusions

This work provided a benchmark study for the laser welding of pure Cu hairpins for the production of electric drives for automotive traction. Six different laser system configurations characterized by different power levels, spots sizes, wavelengths, and beam shaping capabilities were assessed. With all the laser configurations providing keyhole welds with no macro defects, the main quality attribute was the mechanical strength. The work provided a systematic analysis laying the parameters of comparison between the systems and between the weld seams. The main conclusions of the work can be summarized as follows.

- Solid state fiber and disk sources between 3 and 6 kW laser power provide welds of sufficient quality with adequately chosen process parameters. The main performance criteria remain the productivity and the mechanical strength of the welds.
- The 6 kW NIR laser sources with 50 μm delivery fiber provide a rapid process with low energy input and a high penetration depth based on keyhole welding. Other options with lower power or larger beams tend to increase the keyhole welding process time and the energy input independently from the wavelength.
- In source beam dynamic beam shaping should have a matching irradiance profile. The results suggest that the high central core peak should be accompanied by added power to the tail to suppress the spatter together with a high penetration depth.
- The mechanical strength of the weld beads depends mainly on the effective resistant area that is both a function of weld depth and porosity. While all welds have a high fraction of porosity, an increased weld resistant area provides the highest strength.

Along with the observed results the present work underlines the need for standardized testing and qualification. For a universal comparison of the process performance, the need for open benchmarking data remains fundamental. Considering such needs, the future works will assess the influence of the laser stripping phase on the laser welding performance as well as the elaboration of inline monitoring data for defect detection.

CRediT authorship contribution statement

Simone D'Arcangelo: Conceptualization, Methodology, Formal

analysis, Investigation, Data curation, Software, Writing – original draft, Writing – review & editing. **Leonardo Caprio:** Conceptualization, Methodology, Formal analysis, Investigation, Data curation, Software, Writing – original draft, Writing – review & editing. **Davide Chesi:** Conceptualization, Methodology, Investigation, Writing – review & editing. **Daniele Nocciolini:** Conceptualization, Methodology, Investigation, Writing – review & editing. **Rubino Corbinelli:** Methodology, Supervision, Resources, Writing – review & editing. **Barbara Previtali:** Methodology, Supervision, Resources, Writing – original draft, Writing – review & editing. **Ali Gökhan Demir:** Conceptualization, Methodology, Supervision, Formal analysis, Investigation, Writing – original draft, Writing – review & editing.

Declaration of Competing Interest

The authors declare that they have no known competing financial interests or personal relationships that could have appeared to influence the work reported in this paper.

Data availability

Data will be made available on request.

References

[1] R.R. Kumar, K. Alok, Adoption of electric vehicle: A literature review and prospects for sustainability, J. Clean. Prod. 253 (2020), 119911, https://doi.org/10.1016/j.jclepro.2019.119911.

[2] A. Kampker, P. Treichel, K.D. Kreiskother, M. Krebs, M.K. Buning, Ex-Ante Process-FMEA for Hairpin Stator Production by Early Prototypical Production Concepts, 2018 8th Int. Electr. Drives Prod. Conf. EDPC 2018 - Proc. (2019). doi: 10.1109/EDPC.2018.8658288.

[3] A. Arzillo, P. Braglia, S. Nuzzo, D. Barater, G. Franceschini, D. Gerada, C. Gerada, Challenges and Future opportunities of Hairpin Technologies, IEEE Int. Symp. Ind. Electron. (2020) 277–282, https://doi.org/10.1109/ISIE45063.2020.9152417.

[4] A. Riedel, M. Masuch, M. Weigelt, T. Glabel, A. Kuhl, S. Reinstein, J. Franke, Challenges of the Hairpin Technology for Production Techniques, ICEMS 2018 - 2018 21st Int. Conf. Electr. Mach. Syst. (2018) 2471–2476. doi: 10.23919/ICEMS.2018.8549105.

[5] K.M. Hong, Y.C. Shin, Prospects of laser welding technology in the automotive industry: A review, J. Mater. Process. Technol. 245 (2017) 46–69, https://doi.org/10.1016/j.jmatprotec.2017.02.008.

[6] T. Glaessel, D.B. Pinhal, M. Masuch, D. Gerling, J. Franke, Manufacturing influences on the motor performance of traction drives with hairpin winding, 2019 9th Int. Electr. Drives Prod. Conf. EDPC 2019 - Proc. (2019). doi: 10.1109/EDPC48408.2019.9011872.

[7] T. Glaessel, J. Seefried, M. Masuch, A. Riedel, A. Mayr, A. Kuehl, J. Franke, Process Reliable Laser Welding of Hairpin Windings for Automotive Traction Drives, 2019 Int, Conf. Eng. Sci. Ind. Appl. ICESI 2019 (2019) 1–6, https://doi.org/10.1109/ICESI.2019.8863004.

[8] J. Seefried, A. Mahr, M. Weigelt, A. Kuhl, J. Franke, Challenges of Contacting Processes for Thin Copper Flat Wires in the Context of Electromechanical Engineering, 2021 11th Int. Electr. Drives Prod. Conf. EDPC 2021 - Proc. (2021). doi: 10.1109/EDPC53547.2021.9684202.

[9] A. Kampker, K.D. Kreisköther, M.K. Büning, P. Treichel, Challenge of Hairpin Technology Technology Boost for OEMs and Plant Manufacturers, ATZelektronik Worldw. 13 (2018) 54–59, https://doi.org/10.1007/s38314-018-0068-z.

[10] L. Quintino, A. Costa, R. Miranda, D. Yapp, V. Kumar, C.J. Kong, Welding with high power fiber lasers - A preliminary study, Mater. Des. 28 (2007) 1231–1237, https://doi.org/10.1016/j.matdes.2006.01.009.

[11] S.T. Auwal, S. Ramesh, F. Yusof, S.M. Manladan, A review on laser beam welding of copper alloys, Int. J. Adv. Manuf. Technol. 96 (2018) 475–490, https://doi.org/10.1007/s00170-017-1566-5.

[12] M. Hummel, M. Külkens, C. Schöler, W. Schulz, A. Gillner, In situ X-ray tomography investigations on laser welding of copper with 515 and 1030 nm laser beam sources, J. Manuf. Process. 67 (2021) 170–176, https://doi.org/10.1016/j.jmapro.2021.04.063.

[13] M. Miyagi, X. Zhang, Investigation of laser welding phenomena of pure copper by x-ray observation system, J. Laser Appl. 27 (2015), 042005, https://doi.org/10.2351/1.4927609.

[14] W.M. Steen, J. Mazumder, Laser Material Processing (2010), https://doi.org/10.1007/978-1-84996-062-5.

[15] A. Heider, J. Sollinger, F. Abt, M. Boley, R. Weber, T. Graf, High-speed X-ray analysis of spatter formation in laser welding of copper, Phys. Procedia 41 (2013) 112–118, https://doi.org/10.1016/j.phpro.2013.03.058.

[16] M. Miyagi, X. Zhang, Y. Kawahito, S. Katayama, Surface void suppression for pure copper by high-speed laser scanner welding, J. Mater. Process. Technol. 240 (2017) 52–59, https://doi.org/10.1016/j.jmatprotec.2016.09.008.

[17] A. Heider A. Hess R. Weber T. Graf Stabilized copper welding by using power modulated green and IR laser beams, 30th Int Congr. Appl. Lasers Electro-Optics, ICALEO 395 (2011) 395–402. 10.2351/1.5062263.

[18] A. Heider, P. Stritt, A. Hess, R. Weber, T. Graf, Process stabilization at welding copper by laser power modulation, Phys. Procedia 12 (2011) 81–87, https://doi.org/10.1016/j.phpro.2011.03.011.

[19] E. Assuncao, S. Williams, D. Yapp, Interaction time and beam diameter effects on the conduction mode limit, Opt. Lasers Eng. 50 (2012) 823–828, https://doi.org/10.1016/j.optlaseng.2012.02.001.

[20] E. Papastathopoulos, O. Bocksrocker, K. Fiechtner, S. Pricking, R. Flaig, O. Effinger, P. Haug, M. Moeller, T. Gottwald, S.-S. Schad, A. Killi, T. Ryba, Advances in beam shaping of high-power CW lasers with BrightLine weld technology, in: S. Kaierle, S. W. Heinemann (Eds.), High-Power Laser Mater. Process. Appl. Diagnostics, Syst. XI, SPIE, 2022: p. 1. doi: 10.1117/12.2607138.

[21] Trumpf, World premiere at Formnext: green laser from TRUMPF prints copper and gold, (2018). https://www.trumpf.com/it_IT/impresa/stampa/comunicatistampa/comunicato-stampa-pagina-con-i-dettagli/release/world-premiere-at-formnext-green-laser-from-trumpf-prints-copper-and-gold/.

[22] Laserline GmbH, Laserline blue: Diode Lasers for the Processing of High Reflective Metals, (2022). https://www.laserline.com/en-int/blue-3kw-diode-laser/ (accessed June 5, 2022).

[23] A. Singh, L. Caprio, B. Previtali, A.G. Demir, Processability of pure Cu by LPBF using a ns-pulsed green fiber laser, Opt. Laser Technol. 154 (2022), https://doi.org/10.1016/j.optlastec.2022.108310.

[24] M. Haubold, A. Ganser, T. Eder, M.F. Zäh, Laser welding of copper using a high power disc laser at green wavelength, Procedia CIRP. 74 (2018) 446–449, https://doi.org/10.1016/j.procir.2018.08.161.

[25] F. Kaufmann, A. Meier, J. Ermer, Influence of defocusing in deep penetration welding of copper by using visible wavelength, (2021).

[26] M.S. Zediker, R.D. Fritz, M.J. Finuf, J.M. Pelaprat, Laser welding components for electric vehicles with a high-power blue laser system, J. Laser Appl. 32 (2020), 022038, https://doi.org/10.2351/7.0000054.

[27] V. Dimatteo, A. Ascari, P. Faverzani, L. Poggio, A. Fortunato, The effect of process parameters on the morphology, mechanical strength and electrical resistance of CW laser-welded pure copper hairpins, J. Manuf. Process. 62 (2021) 450–457, https://doi.org/10.1016/j.jmapro.2020.12.018.

[28] M. Omlor, N. Seitz, T. Butzmann, T. Petrich, R. Gräf, A.C. Hesse, K. Dilger, Quality characteristics and analysis of input parameters on laser beam welding of hairpin windings in electric drives, Weld. World. (2023), https://doi.org/10.1007/s40194-023-01500-y.

[29] C. Franz, O. Bruchwald, Process Monitoring in E-Mobility Applications, PhotonicsViews. 17 (2020) 64–68, https://doi.org/10.1002/phvs.202000029.

[30] M. Baader, A. Mayr, T. Raffin, J. Selzam, A. Kuhl, J. Franke, Potentials of Optical Coherence Tomography for Process Monitoring in Laser Welding of Hairpin Windings, in: 2021 11th Int. Electr. Drives Prod. Conf., 2021: pp. 1–10. doi: 10.1109/edpc53547.2021.9684210.

[31] J. Hartung, A. Jahn, O. Bocksrocker, M. Heizmann, Camera-based in-process quality measurement of hairpin welding, Appl. Sci. 11 (2021), https://doi.org/10.3390/app112110375.

[32] A. Mayr, L. Hauck, M. Meiners, J. Franke, Prediction of the Joint Cross-Section of Laser-Welded Hairpin Windings Based on 2D Image Data Using Convolutional Neural Networks, 2020 10th Int. Electr. Drives Prod. Conf. EDPC 2020 - Proc. (2020). doi: 10.1109/EDPC51184.2020.9388193.

[33] J. Vater, M. Pollach, C. Lenz, D. Winkle, A. Knoll, Quality control and fault classification of laser welded hairpins in electrical motors, Eur. Signal Process. Conf. 2021-Janua (2021) 1377–1381, https://doi.org/10.23919/Eusipco47968.2020.9287701.

[34] D.C. Montgomery, Design and Analysis of Experiments, 7th Edition, 2009.

[35] R. Monroe, Porosity in castings, AFS Trans. 113 (2005) 519–546.

[36] H.C. Chen, G. Bi, M.L.S. Nai, J. Wei, Enhanced welding efficiency in laser welding of highly reflective pure copper, J. Mater. Process. Technol. 216 (2015) 287–293, https://doi.org/10.1016/j.jmatprotec.2014.09.020.

[37] N. Eisenreich, M. Aeckerle, C. Bantel, A. Heider, A. Olowinsky, Influence of laser parameters on tensile shear strength of copper welds, J. Laser Appl. 31 (2019), 022411, https://doi.org/10.2351/1.5096094.

[38] R. Fabbro, Melt pool and keyhole behaviour analysis for deep penetration laser welding, J. Phys. D Appl. Phys. 43 (2010), https://doi.org/10.1088/0022-3727/43/44/445501.

[39] L. Wang, M. Mohammadpour, X. Gao, J.P. Lavoie, K. Kleine, F. Kong, R. Kovacevic, Adjustable Ring Mode (ARM) laser welding of stainless steels, Opt. Lasers Eng. 137 (2021), https://doi.org/10.1016/j.optlaseng.2020.106360.

[40] L. Panasonic Industry Co., Blue Direct Diode Laser / Laser Welding Robots, (2022). https://industrial.panasonic.com/ww/products-fa/welding/industrial-robots/laser-welding-cutting-robot (accessed June 5, 2022).

[41] Laserline GmbH, On welding copper components, (2022).

[42] O. Bocksrocker, N. Speker, M. Beranek, T. Hesse, Reduction of spatters and pores in laser welding of copper hairpins using two superimposed laser beams, Lasers Manuf. Conf. 2019 Reduct. (2019) 1–8.

[43] H. Yang, X. Tang, C. Hu, S. Liu, Y. Fan, Y. Xiao, G. Lu, Q. Wang, G. Chen, P. Xing, H. Tan, Z. Guo, Z. Niu, Study on laser welding of copper material by hybrid light source of blue diode laser and fiber laser, J. Laser Appl. 33 (2021), 032018, https://doi.org/10.2351/7.0000386.

[44] M. Mohammadpour, L. Wang, F. Kong, R. Kovacevic, Adjustable ring mode and single beam fiber lasers: A performance comparison, Manuf. Lett. 25 (2020) 50–55, https://doi.org/10.1016/j.mfglet.2020.07.003.

[45] T. Glaessel, J. Seefried, A. Kuehl, J. Franke, Skinning of insulated copper wires within the production chain of hairpin windings for electric traction drives, Int. J. Mech. Eng. Robot. Res. 9 (2020) 163–169, https://doi.org/10.18178/ijmerr.9.2.163-169.

[46] J. Vater, M. Kirschning, D. Scheurenberg, D. Abel, A. Knoll, Development of a Cloud- And Edge-Architecture for adaptive model weight optimization of a CNN exemplified by optical detection of hairpin welding, 2020 10th Int. Electr. Drives Prod. Conf. EDPC 2020 - Proc. (2020). doi: 10.1109/EDPC51184.2020.9388192.

[47] M. Garavaglia, A.G. Demir, S. Zarini, B.M. Victor, B. Previtali, Fiber laser welding of AA 5754 in the double lap-joint configuration: process development, mechanical characterization, and monitoring, Int. J. Adv. Manuf. Technol. 111 (2020) 1643–1657, https://doi.org/10.1007/s00170-020-06128-6.